

# High Numerical Aperture Hexagonal Stacked Ring-Based Bidirectional Flexible Polymer Microlens Array

Rajib Ahmed,<sup>\*,†</sup> Ali K. Yetisen,<sup>‡,§</sup> and Haider Butt<sup>\*,†</sup>

<sup>†</sup>Microengineering and Nanotechnology Laboratory, School of Engineering, University of Birmingham, Birmingham B15 2TT, United Kingdom

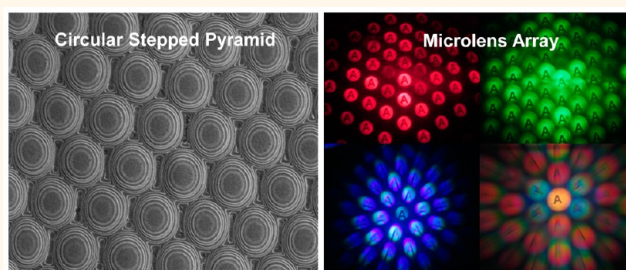
<sup>‡</sup>Harvard Medical School and Division of Biomedical Engineering, Brigham and Women's Hospital, 65 Lansdowne Street, Cambridge, Massachusetts 02139, United States

<sup>§</sup>Harvard–MIT Division of Health Sciences and Technology, Massachusetts Institute of Technology, 65 Lansdowne Street, Cambridge, Massachusetts 02139, United States

## S Supporting Information

**ABSTRACT:** Flexible imprinted photonic nanostructures that are able to diffract/focus narrow-band light have potential applications in optical lenses, filters, tunable lasers, displays, and biosensing. Nanophotonic structures through holography and roll-to-roll printing may reduce fabrication complexities and expenses and enable mass production. Here, 3D photonic nanostructures of a stacked ring array were imprinted on acrylate polymer (AP) over poly(ethylene terephthalate) (PET) substrate through holography and lift-off processes to create a microlens array (MLA). The surface structure of the array consisted of circular nonstepped pyramids, and repeated patterns were in hexagonal arrangements. Stacked-ring-based MLA (SMLA) on a flexible AP–PET substrate showed efficient bidirectional light focusing and maximum numerical aperture (NA = 0.60) with a reasonable filling factor. The nanostructures produced a well-ordered hexagonally focused diffraction pattern in the far field, and power intensities were measured through angle-resolved experiments. The variation of nanostep dimensions (width and height) and the number of steps resulted in different photonic bandgaps, and the arrays produced distance-dependent narrow-band light focusing. The validation of the SMLA was demonstrated through the text, image, and hologram projection experiments. It is anticipated that imprinted bidirectional SMLA over flexible substrates may find applications in optical systems, displays, and portable sensors.

**KEYWORDS:** microlens array, photonics, stacked rings, bidirectional focusing, diffraction grating



Microlens array (MLA) is an ordered collection of two/three-dimensional (2D/3D) photonic lenses having aperture sizes less than a few millimeters.<sup>1,2</sup> In 1665, Robert Hooke first used melted rods as small lenses to study insects.<sup>3</sup> In the 1940s, Dennis Gabor proposed an array of microscale lenses as superlenses to go beyond the diffraction limit.<sup>4</sup> Gabor's superlenses are now widely used as microlens arrays having application in beam shaping, optical interconnections or coupling, photolithography, and imaging.<sup>5,6</sup> Microlens arrays became essential components of many optical components such as charge-coupled devices (CCDs) cameras or sensors, fiber couplers, optical switches, and light-emitting-diodes (LEDs) or organic-LED (OLED) systems.<sup>7,8</sup> Microlens arrays can be fabricated by lithography, ion-beam writing, wet etching, stamping or embossing, photoresist reflow, UV replication, or inkjet imprinting.<sup>9,10</sup> However, most of the

microlenses manufacturers adopted lithography, ion-exchange, or diamond point tuning techniques to produce high-quality lenses. However, the cost of these fabrication techniques is high, and the features of these microlenses are limited in diameter and focal length.<sup>5,11</sup> Microlenses have been also fabricated using graphene, liquid crystals, photonic crystals, hydrogels, and polymers.<sup>12–19</sup> Microlens structures have been fabricated in square, circular, octagonal, diamond, stacked circle, and honeycomb arrangements.<sup>13,15,20–23</sup> However, uniform and accurate geometries of MLAs are desired for efficient light focusing in optical applications.<sup>24</sup> Previously reported MLA fabrication techniques including reflow or transfer methods

Received: January 10, 2017

Accepted: February 27, 2017

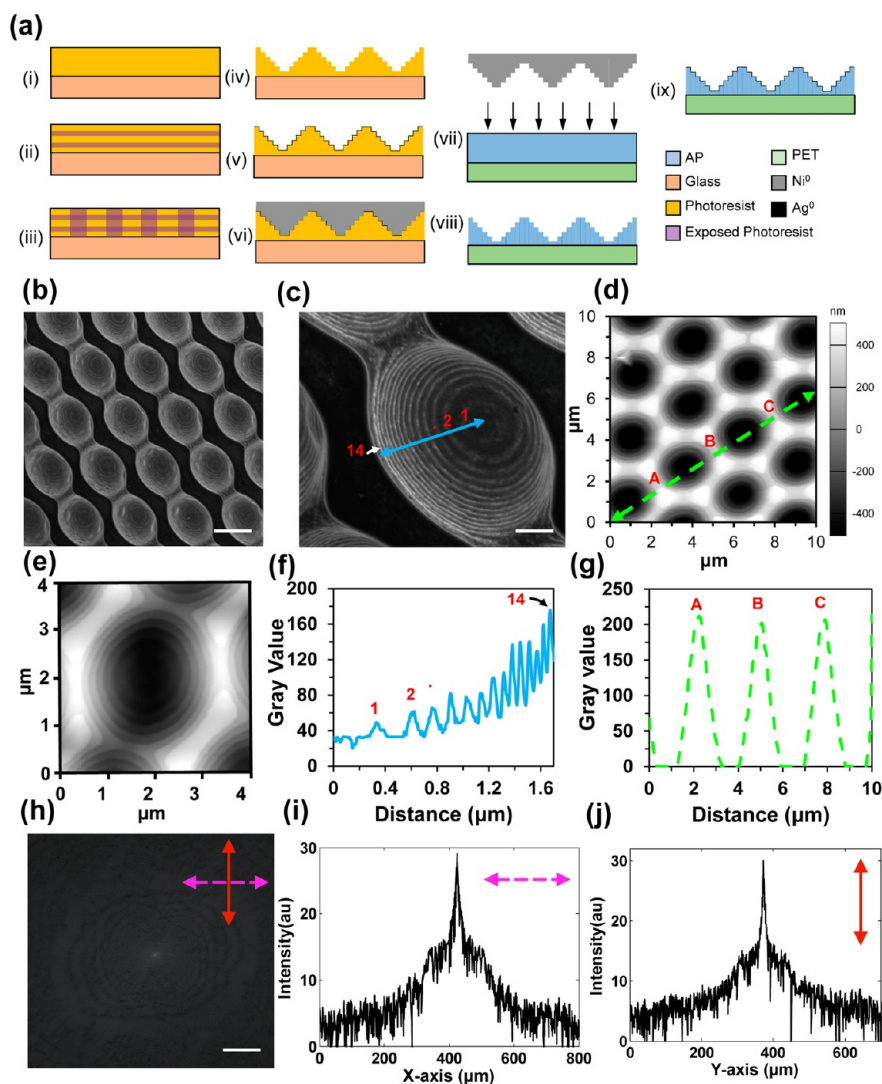


**Figure 1.** Fabrication and characterization of SMLAs. (a) Fabrication steps of the SMLA. (b, c) SEM image of array and a single magnified cell consisting of circular stepped concavities. Scale bar = 2.0 and 0.4  $\mu\text{m}$ . (d) AFM image of the array and a single cell of the SMLA. (e) Surface (gray value) profile of the steps and height of a single cell of a SMLA. (f) Gray value profile of a SMLA. (g) FFT of the fabricated single cell of a SMLA. Scale bar = 100  $\mu\text{m}$ . (h, i) Simulated focused light along  $x$  and  $y$  axes of the fabricated sample.

were limited in light-focusing capability and numerical aperture (NA) values ( $<0.40$ ).<sup>25,26</sup> Therefore, it is challenging to produce high-resolution images from microscopic objects. Inkjet-printed MLAs (NA:  $<0.50$ ) were also reported.<sup>27,28</sup> This approach required high-cost setups and polymer-coated substrates. Recently, MLAs (NA:  $<0.56$ ) were fabricated with laser ion-beam patterning and direct laser ablation.<sup>1,29</sup>

Laser ablation based holographic laser interference lithography has been used to efficiently produce a surface-relief MLA.<sup>30</sup> This approach is fast, eliminates complex and tedious pre/post-treatment of samples, is cost-effective, and does not require high technical expertise.<sup>14,31</sup> Direct laser interference lithography (DLIL) is based on in-line or off-line laser interference techniques and does not require masks for the 2/3D surface patterning.<sup>32</sup> DLIL-based patterning is mainly based on UV, femtosecond (fs), and nanosecond (ns) laser ablation techniques to create submicron nanophotonic structures.<sup>33–37</sup> Surface patterning based on a fs-laser involves short pulse duration to ablate a wide range of materials where thermal conduction can be neglected (direct solid to plasma state).<sup>38</sup> Laser ablation based on ns-laser patterning allows printing of

holographic devices, offering low cost and less production complexity.<sup>31</sup> Single beam or multibeam laser light has been utilized to produce interference patterns to ablate 2D/3D nanopatterns.<sup>30,32,39–42</sup> Laser ablation can be utilized to form nanophotonic devices in ink, gold, polymers, or functionalized substrates.<sup>35,42–45</sup> The patterned geometries depend on the laser properties (ablation energy, laser wavelength, spot size) and structural parameters (distance, height, and recording angle).<sup>31,35</sup> However, multibeam interference require precise exposure angles to create complex nanostructures.<sup>39</sup>

Here, 3D-stacked rings in a hexagonal arrangement were produced through multibeam interference based holography, and copies were imprinted through roll-to-roll processing over large areas of a flexible polymeric film. The patterned photonic nanostructures focused light and acted as SMLA. The optical-focusing property of the SMLA was experimentally characterized, and computational modeling was performed to understand their optical properties. The SMLA showed efficient bidirectional focusing property and maximum NA of  $\sim 0.60$ . The performance of the SMLA was analyzed by varying its structural parameters (step width, height, and number of

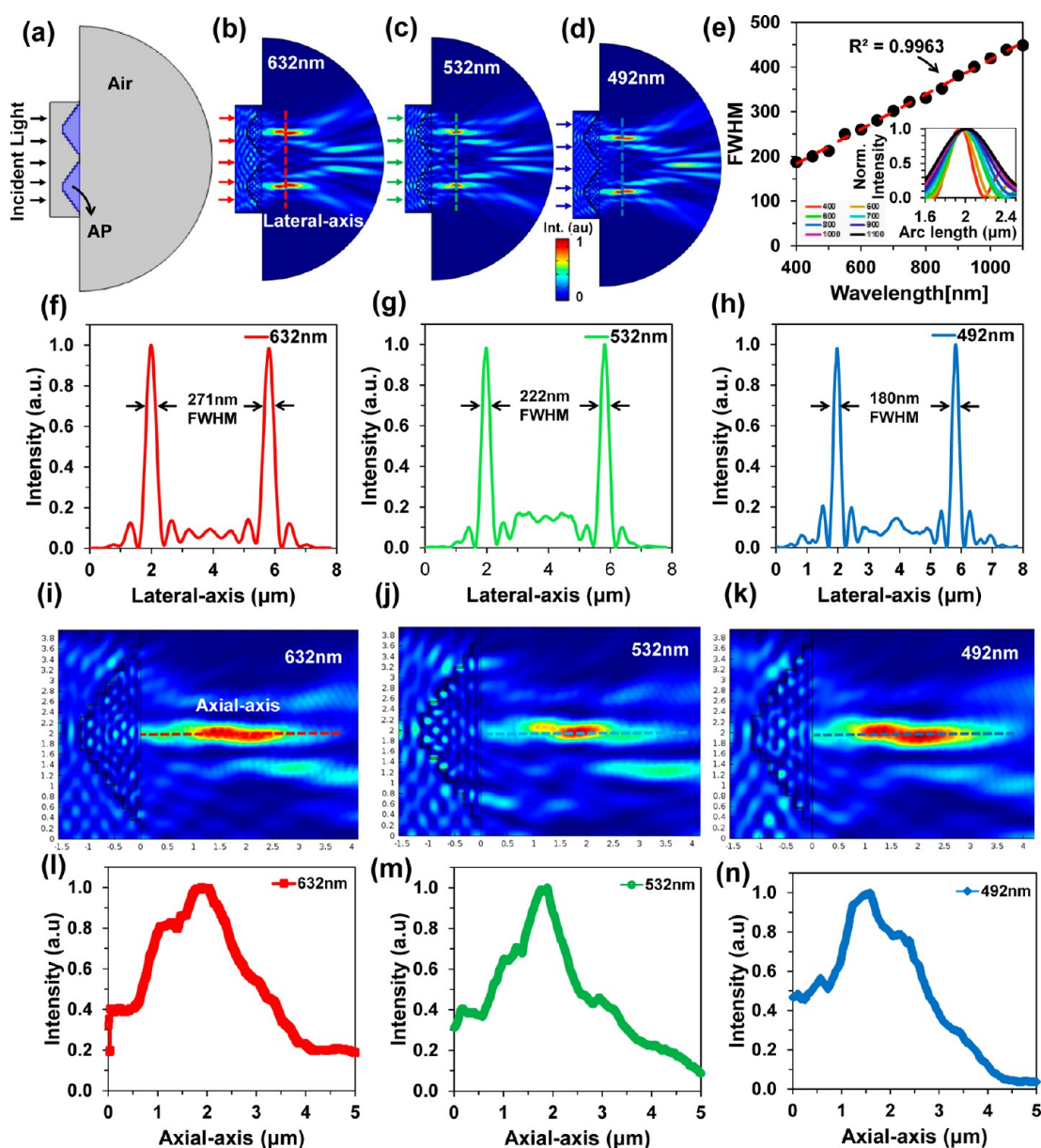


**Figure 2.** Computational modeling of SMLA and their optical properties. (a) Geometry of a modeled SMLA designed with circular stepped concavities. (b–d) Electric field distribution of the focused light for red, green, and blue light illumination. (e) fwhm of the focused light as a function of wavelength. (f–h) Normalized intensity (along lateral axis) of the focused light for the monochromatic light illumination. (i–k) Magnified electric field distribution of the focused light for the monochromatic light illumination on a single cell of SMLA. (l–n) Normalized intensity (along axial axis) of the focused light for monochromatic light illumination.

steps). Far-field experiments showed focused multiorder diffraction patterns in a hexagonal configuration. Angle-resolved light intensity measurements were also performed through 3D rotation stages. The projection experiments with monochromatic (red, green, and blue) and broadband light illumination through text and holograms showed multiple images at the far field, which verified that sample acted as a MLA. The uniformity of the surface roughness and truncated nanosteps ensured high quality and brightness of the focused images.

## RESULTS AND DISCUSSION

**SMLA Fabrication and Optical Parameters.** The fabrication of the SMLA consisted of subsequent photoresist patterning stages.<sup>32</sup> Positive photoresist (diazonaphthoquinone) was spin-coated over a glass substrate (1.0 mm) at

100 rpm for 2 min and baked at 80 °C for 1 h (Figure 1a(i)). The nanostep surface patterning over the positive photoresist (thickness  $\sim 1.2 \mu\text{m}$ ,  $n = 1.65$ ) was performed with (a) multilayer exposure (prism coupling) and (b) opening exposure steps. During prism coupling, the circular-stepped holographic multilayer nanostep patterns were created with interference lithography in photoresist. A triangular prism (gadolinium gallium garnet) was placed over the glass substrate, and an index matching liquid (xylene,  $n = \sim 1.50$ , 1 mL) was deposited between them. An argon-ion laser beam ( $\lambda = 458 \text{ nm}$ , 100 mW,  $\Phi = 14 \text{ cm}$ ) was illuminated (exposure angle  $50^\circ$ , duration  $\sim 1 \text{ min}$ ) over the prism-coupled photoresist layer. Therefore, multilayer interference patterns in the photoresist were created due to total internal reflection effect within the prism–photoresist–air interface (Figure 1a(ii)). The second

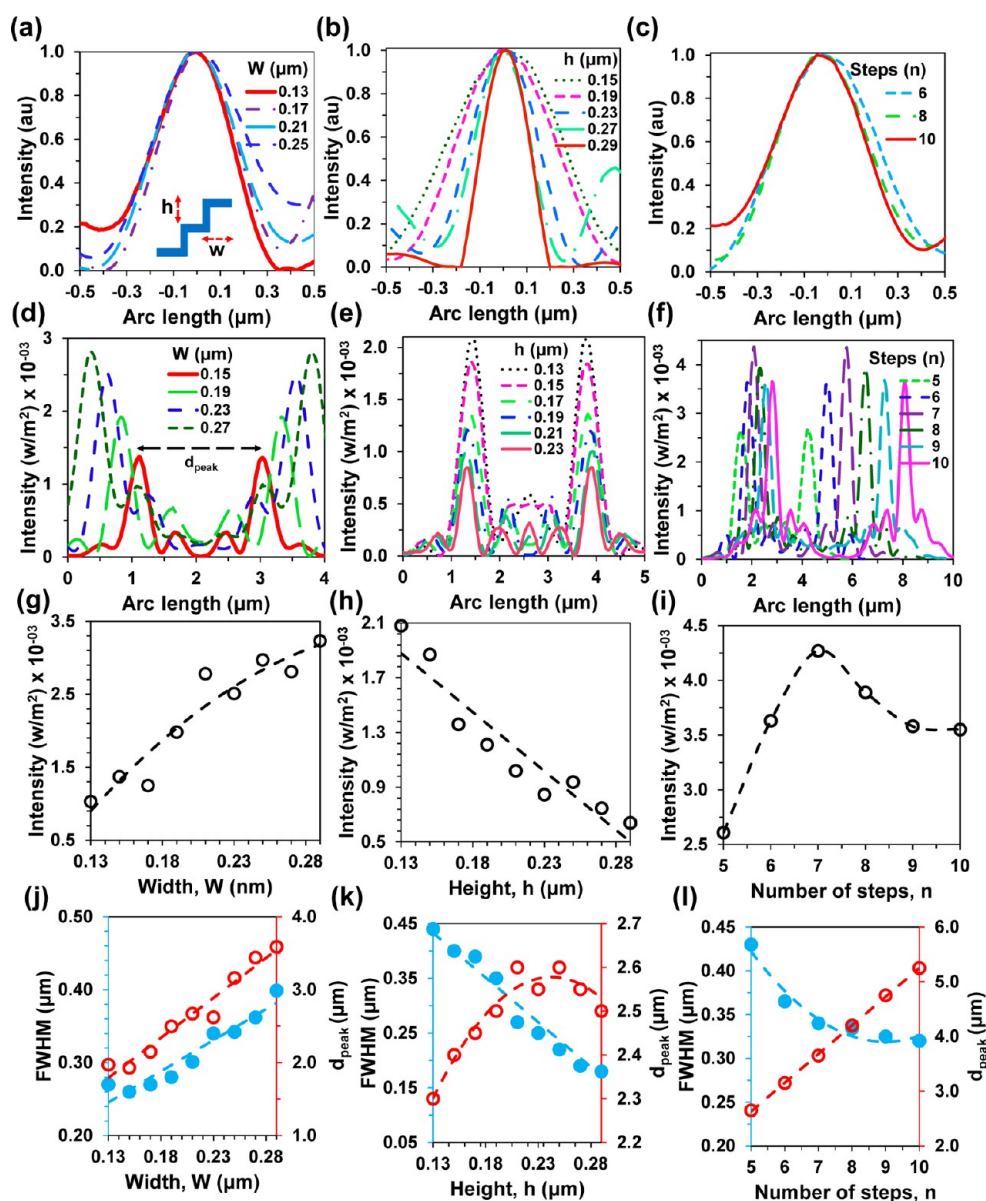


**Figure 3.** Optical properties (along lateral axis) of SMLA with structural parameters variation (width, height, and number of steps). (a–c) Bandwidth of the focused light intensity as a function of structural parameter variation. (d–f) Peak-to-peak distance,  $d_{\text{peak}}$ , of the focused light intensity as a function of structural parameters variation. (g–i) Diffracted normalized intensity as a function of structural parameters variation. (j–l) fwhm and  $d_{\text{peak}}$  as a function of structural parameter variation.

opening exposure stage was used to create hexagonally arranged nanostep patterns. Three azimuthal beams ( $120^\circ$ ) were interfered over the photoresist for 1 min.<sup>22,46</sup> The structural block diagram of the three-beam laser exposure system is also shown in the Supporting Information (Figure S1).<sup>22</sup> The laser beam ( $\lambda = 458$  nm, 100 mW,  $\varnothing = 14$  cm) passes through a variable beam splitter, BS1 (2/3:1/3). The BS1 divides the input beam in two paths (P): two-thirds of the light passes through P1 and finally through BS2 (1/3:1/3). The remaining one-third of the light passes through P2 through a series of mirror setups. The BS2 divides input light into two equal parts and passes through P3 and P4. Therefore, P2, P3, and P4 carry one-third of the input laser light and pass through the pinhole of the spatial filters and lenses (FL). The light through P2 and P3 passes through an optical phase-shift (PS) to provide three azimuthal beams ( $120^\circ$ ) of laser interference onto the target material (photoresist sample). Therefore, lateral and horizontal

interference patterns in hexagonal arrangements are created in the photoresist layer (Figure 1a(iii)). The photoresist patterns were etched using a photographic developer (Figure 1a(iv)). The photoresist pattern was deposited with a silver layer, and a nickel master honeycomb hologram was created using electroplating for the replication of the nanostructures (Figure 1a(v–vi)). Embossed master patterns were transferred on AP-PET substrate using nanoimprinting (Figure 1a(vii)). The replicated pattern consisted of circular nanostructures (Figure 1a(viii)). Finally a  $\sim 3$  nm thin aluminum layer was deposited on the AP-PET substrate through an evaporation process (Figure 1a(ix)).

The scanning electron microscope (SEM) image of the fabricated sample showed a circular stepped structure, resembling pyramids found in Guachimontones, Mexico (Figure 1a,b). The atomic force microscope (AFM) image of the fabricated sample illustrated the depth ( $h$ ,  $\sim 1$   $\mu\text{m}$ ) of the

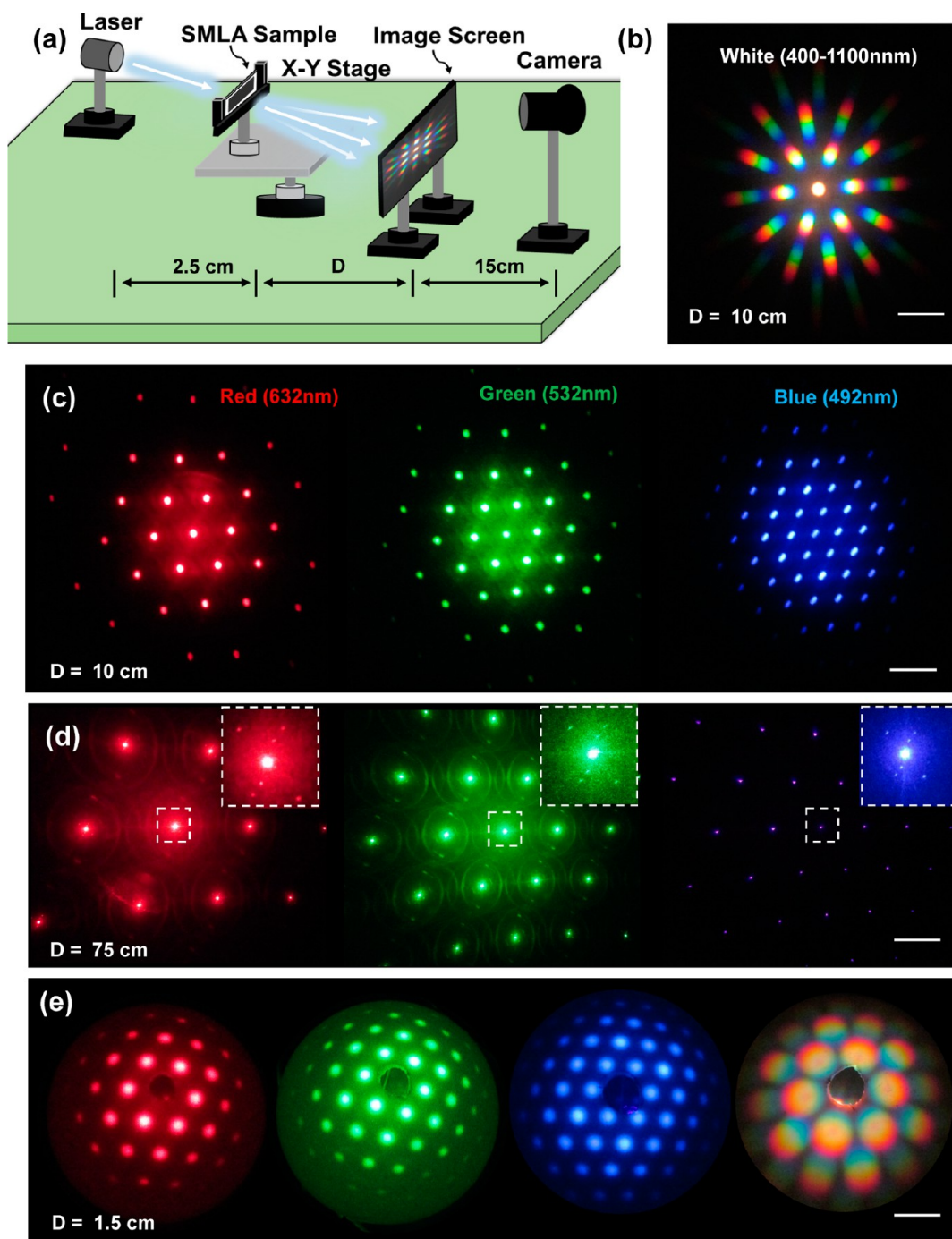


**Figure 4.** Far-field diffraction patterns of a SMLA. (a) Experimental setup for the far-field projection experiments. Distance ( $D$ ): 10, 75, and 1.5 cm. (b–d) Hexagonal diffraction patterns with broadband, red, green, and blue laser illumination. Scale bars = 2.5 cm, and 10.0 cm, respectively. (e) Far-field diffraction experiments with monochromatic and broadband light in a hemispherical surface. Scale bar = 5 cm.

pyramids (Figure 1c,d). The SEM image of the sample cross section had a lens radius  $r \sim 1.8 \mu\text{m}$  and 14 steps (Figure 1e). However, the top seven to eight steps had heights of  $\sim 200 \text{ nm}$  and widths of  $\sim 250 \text{ nm}$ . The distance/pitch of lenses was  $\sim 2.5 \mu\text{m}$  (Figure 1f). The fabricated microlens size depended on the nanostep radius ( $r$ ) and height ( $h$ ), which were used to estimate lens parameters based on geometry and theory: the radius of curvature ( $R$ ), focal length ( $f$ ),  $f$  number ( $f_{\#}$ ), and numerical aperture (NA) using the following relations<sup>10,14,20</sup>

$$R = (h^2 + r^2)/2h, \quad f = R/(n - 1), \quad f_{\#} = f/2r, \\ \text{NA} = D/2f \quad (1)$$

where  $D$  is the lens diameter ( $2r$ ),  $n$  is the refractive index of the lens material, and  $h < r$ . For the fabricated SMLA, we had  $h = 1.0 \mu\text{m}$ ,  $D = 3.6 \mu\text{m}$ ,  $n = 1.49$  for AP, and  $n = 1.57$  for PET, respectively. Therefore, estimated lens parameters were  $R = 1.78 \mu\text{m}$ ,  $f = 3.1 \mu\text{m}$ ,  $f_{\#} = 0.87$ , and  $\text{NA} = 0.6$ , respectively. The focal length ( $f$ ) of the fabricated SMLA was measured through optical microscopy (Supporting Information, Figure S2). The  $f$  number indicates the light gathering capability of the MLA,

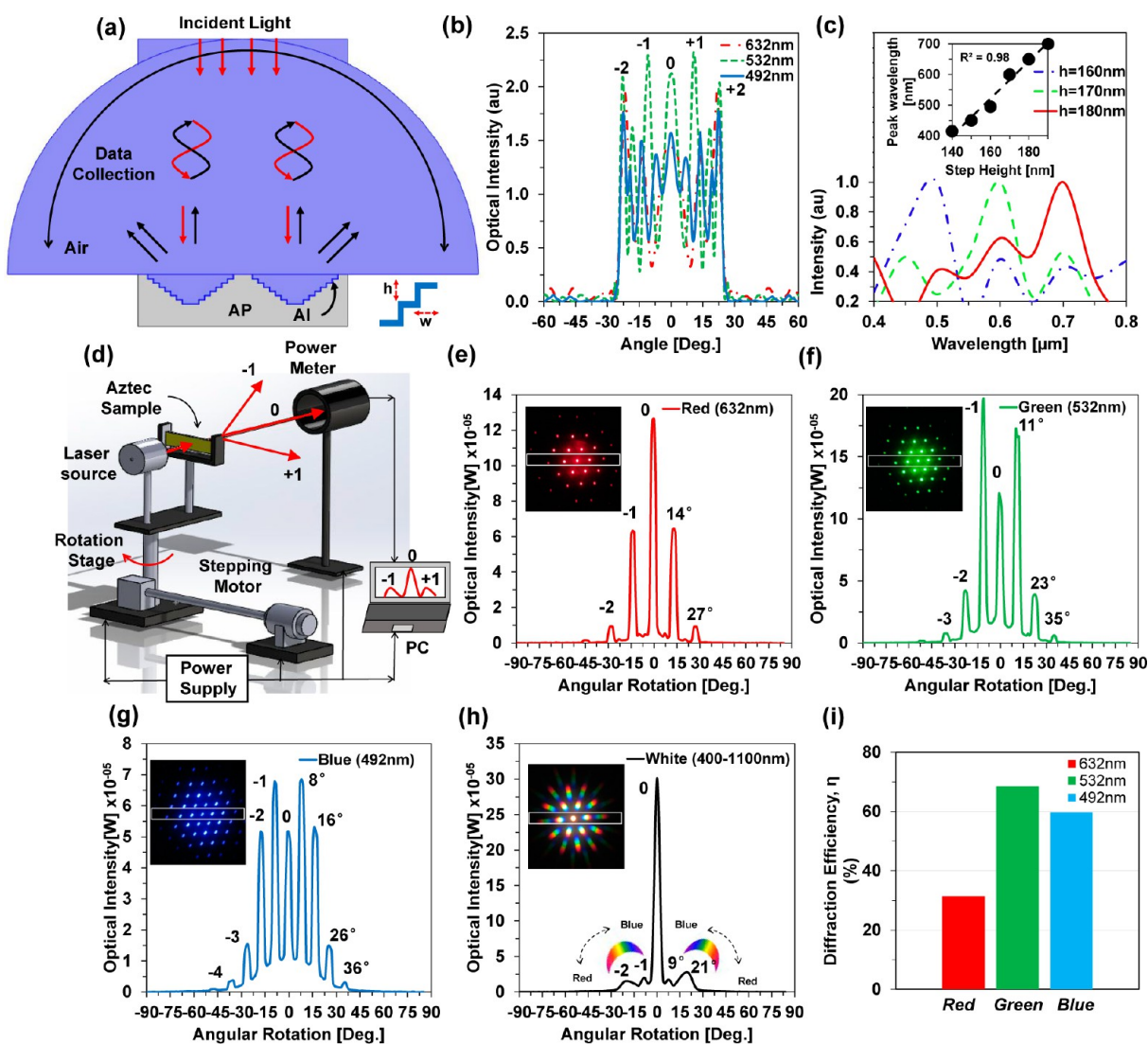


**Figure 5.** Computational modeling and experimental diffraction measurements of a SMLA. (a) Geometry of a modeled SMLA designed with circular stepped concavities for the diffraction analyses. (b) Simulated diffraction curves with red, green, and blue beam illumination. (c) Simulated far-field diffraction intensity as a function of step height. (d) Experimental setup for angle-resolved diffraction measurement of the SMLA. (e–h) Measured optical intensity as a function of angular rotation with monochromatic and broadband light illumination. (i) DE measurements of a SMLA with monochromatic light illumination.

where the lower the value the higher the capability to gather the light. Moreover, NA also shows the light-gathering capability and resolving fine specimen detail at a fixed distance.<sup>29</sup> MLA with high NA collect enough light to provide bright images, and therefore, higher values are desired. The fabricated SMLA showed lower  $f_{\#}$  and higher NA values as compared with other reported MLAs.<sup>13,14,47</sup> Lower  $f_{\#}$  and higher NA values of the MLA strongly depend on width and height variation, which can be controlled through laser exposure angle. Light focusing property of the fabricated MLA sample was computationally estimated before optical characterization. Fast Fourier transform (FFT) of the sample showed far-field diffraction and the bright focusing (Figure 1g). Light intensity along horizontal and vertical axis had sharp focusing at the center of the lenses (Figure 1h,i).

**Computational Modeling of SMLA.** The diffraction from the SMLA was modeled using the finite element method (FEM) based on commercial COMSOL Multiphysics software.<sup>48,49</sup> The model consisted of a 2D geometry of stepped

pyramids with spacing on the order of  $3 \mu\text{m}$  (Figure 2a). The pyramids were made of AP on PET film coated with a 30 nm thick Al layer. The refractive index of the Al layer was  $1.26 + i7.27$  (at 632 nm). The bulk material of the pyramids was defined as PETAP having a refractive index of 1.49. The unit cell of the geometry consisted of two circular stepped pyramid structures with periodic boundary conditions placed across the edges.<sup>35</sup> A hemisphere screen was placed on top of the grating layer, and the area within the hemisphere was defined as air. For simplicity, a 2D simulation was performed and maximum triangular mesh size was one tenth of the input light. The simulated mesh consisted of 35800 domain elements and 1722 boundary elements, and the number of degrees of freedom solved was 25162. A monochromatic light wave was normally illuminated from the left side toward the grating surface. Diffracted light from the nanosteped pyramids focused the light on the right side of the grating (Figure 2a). Simulated results showed well-ordered symmetric light intensity focusing for the red (632 nm), green (532 nm), and blue (492 nm)

wavelengths (Figure 2b). As the wavelength increased, the focal point of the lens and full width half-maximum (fwhm) values (3 dB bandwidth) also increased (Figure 2b–d). The fwhm values linearly shifted to the larger values as the wavelength increased. The observation plane along the lateral axis showed high intensity focusing at focal points for the red, green, and blue wavelengths (Figure 2f–h). The magnified E-field intensity distribution showed that nonuniform focusing of the light along the axial axis (Figure 2i–k). Moreover, normalized intensity distribution of the vertical axis was wider as compared to the lateral axis (Figure 2i–k). Simulations were performed through the front side of the SMLA models, where the stepped rings faced the incident light. However, SMLAs also showed efficient light focusing at the back side (stepped rings opposite side of the incident light) and acted as bidirectional SMLAs (Supporting Information, Figures S3 and S4).

The light focusing from the SMLAs was due to the stepped nanostructures. The structural parameters (step width, height, and number of steps) tailor the light propagation properties and produce constructive interference at the focal point. Computational studies were performed for the focusing properties of SMLAs by varying the geometry. The focused light's bandwidth (BW) became wider as the step width increased (Figure 3a). However, the BW decreased as the step height and the number of steps increased (Figure 3b,c). The peak-to-peak focused light distance ( $d_{\text{peak}}$ ) increased as the width and number of steps increased (Figure 3d, f). However,  $d_{\text{peak}}$  increased up to a certain range then decreased as height increased (Figure 3e). The focused light intensity increased as the step width increased, but intensity decreased as the step height decreased (Figure 3g,h). Additionally, the intensity increased up to seven steps, and it decreased as the number of steps increased (Figure 3i). Figure 3j–l shows fwhm and  $d_{\text{peak}}$  as functions of step width, height, and the number of steps.

**Optical Properties of SMLAs.** Optical characterization of the patterned SMLA was performed through monochromatic and broadband light-diffraction experiments. The far-field focused diffraction patterns were also visualized using an image screen setup (Figure 4a). Similar diffraction patterns from a hexagonal MLA were previously reported.<sup>50</sup> The incident light normally illuminated the sample, and an image screen was placed behind the sample. For the broadband light illumination, multiple rainbow patterns in a hexagonal arrangement were observed surrounding the nondiffracted broadband light (zero-order) (Figure 4b). Red and blue light on the rainbow pattern diffracted to the long and short distances, respectively. The diffracted rainbow patterns of the SMLA were analogous to a diffraction grating. The far-field diffractions of the SMLA were demonstrated with red, green, and blue beams (Figure 4c–e). The experiments performed by normally illuminating the SMLA from the front and back sides showed efficient bidirectional focusing.

Hexagonal diffraction patterns were also observed for the monochromatic light beams. The diffraction distances from the center spot increased as the wavelength increased. Therefore, longer distances of the hexagonal diffraction patterns were observed for the red light illumination and blue laser showed shorter diffraction spots, obeying Bragg's law ( $\Lambda = \lambda/2\sin \Theta$ , where  $\Lambda$  is the grating spacing,  $\lambda$  is the wavelength, and  $\Theta$  is the tilt angle from the surface plane). Each hexagonal diffraction spot showed 2D square patterns at longer distances ( $D2 = 7.5$  cm). This may be due to 2D periodic variation of nanosteps and widths. Each of the stepped pyramid circles focuses light at

the center, and at a glance the whole sample acts as a diffractive MLA. Focused diffraction spots were in a hexagonal arrangement. This is due to the hexagonal arrangement of stepped circular pyramid lens concavities during device fabrication. Furthermore, far-field diffraction patterns were also observed on the hemispherical surface for red, green, and blue light illumination. Hexagonal diffraction patterns of the focused light were observed at short distances ( $D2 = 1.5$  cm).

The focused diffraction property of SMLAs was computationally modeled. A monochromatic light illuminated the SMLAs normally from the top (Figure 5a). The diffracted light was collected from a hemispherical boundary surface. Finite-element simulations showed well-ordered symmetrical diffraction patterns for the red (632 nm), green (532 nm), and blue (492 nm) light (Figure 5b). Shorter and longer diffraction distances were found with green and blue laser illumination of the stepped grating surface. The number of diffraction orders increased with blue laser illumination. The red beam showed less diffraction orders (second orders) as compared to blue light (fourth orders). The diffracted light intensity color strongly depended on the step height of the pyramid. As the step height increased, the diffracted color wavelength linearly shifted to the longer wavelengths (Figure 5c). Furthermore, the angle-resolved diffraction measurements of the fabricated stepped grating were performed by using a 3D rotation stage (Figure 5d). Stepped grating was placed in the  $x$ – $y$  position stage, and the incident light was used to perpendicularly illuminate the grating surface, where distance to a spectrophotometer probe was varied. The laser pointer and sample holder stage was controlled with a stepper motor which could rotate  $360^\circ$  ( $1^\circ$  step size). The optical powermeter probe was placed normal ( $0^\circ$ ) to the sample for intensity measurements. Figure 5e–h shows diffraction intensity as a function of rotation angle for red, green, blue, and broadband light illumination. The diffracted focused light intensity was measured along the  $x$ -axis (Figure 5e–h insets) through the optical powermeter. The diffraction distance from the central spot increased as the incident light wavelength increased. Therefore, the diffracted focused light in a hexagonal arrangement for the red light showed maximum radii as compared with blue light. Green and blue beams resulted in light diffraction up to three and four orders, respectively. Similarly, increased diffraction orders were also found at shorter wavelengths in the simulated model, agreeing with the experimental results (Figure 5b). The diffraction efficiency (DE), which was the ratio between diffracted ( $P_{\text{diff}}$ ) and incident ( $P_{\text{inc}}$ ) lights, was calculated for the red, green, and blue beams (Figure 5i).<sup>31</sup> The maximum DE was found with green laser (70%), and red laser showed minimum DE (30%).

The optical-focusing property of the SMLA was tested with an optical microscope arrangement (Figure 6a). The microscope was in transmission mode, and the SMLA was placed in a sample holder stage. The broadband light illuminated the sample from the backside of a glass slide. An objective lens ( $\times 20$ ,  $NA = 0.40$ ) of the microscope system was placed on the opposite side of the light source. A CCD camera was used to capture the microscopic images. The sample stage was moved along the  $z$ -axis to measure the focal point,  $f = 3 \mu\text{m}$  ( $z = 0$ ), which was in agreement with the simulated diffraction model. The focal point was measured from the distance between the completely unfocused ( $\pm z$ ) upper point and lower focus point ( $z = 0$ ) (Supporting Information, Figure S2).<sup>21</sup> Transmission intensity of the SMLA was measured for the broadband light

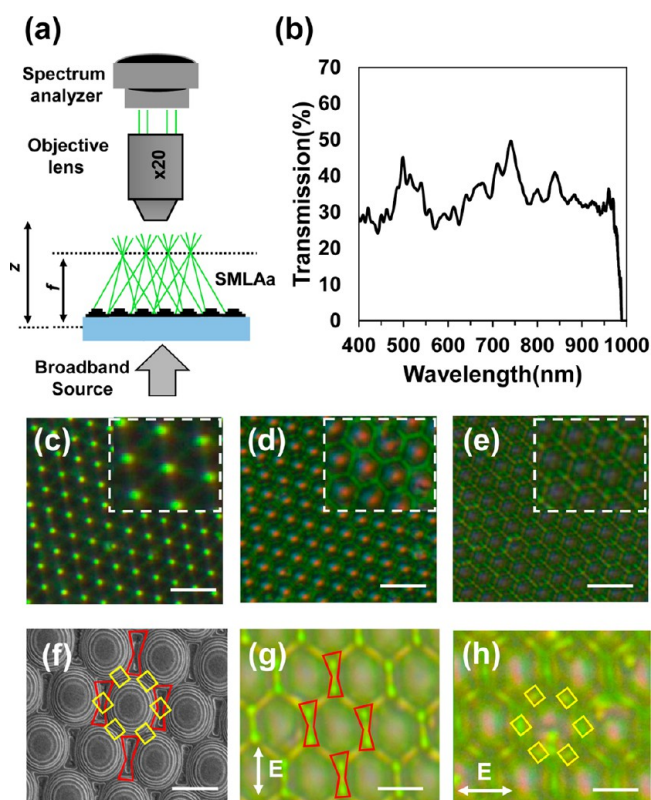


**Figure 6.** Optical properties of an SMLA with broadband light illumination. (a) Computational block diagram of the focusing property measurement of the SMLA. (b) Transmission properties of the SMLA with broadband light illumination. (c) Focusing green light with broadband light illumination using SMLA. Scale bar = 10  $\mu\text{m}$ . (d, e) Red and blue light are at the center of each concavity of SMLA during unfocused conditions. Scale bars = 10  $\mu\text{m}$ . (f) Electron microscope image of an SMLA and hot-spot areas. Scale bar = 2  $\mu\text{m}$ . (g, h) Polarization-dependent green hotspots during unfocused conditions. Scale bar = 2  $\mu\text{m}$ .

illumination (Figure 6b). Maximum transmission peaks were observed for the green and red wavelengths. For broadband light illumination, green light was mainly focused at the focal point (Figure 6c). However, red and blue colors were at the center of the stepped circles at unfocused conditions due to chromatic aberration effect (Figure 6d,e). During unfocused conditions, a localized light polarization effect was also observed. Polarization-selective green hotspots were found between the stepped rings (Figure 6f). For the  $x$ -polarized light, green hotspots were at each point of the hexagonal cells. For  $y$ -polarized light, the green spots were at the middle points of each arm of the hexagonal cells.

The optical property of the SMLA was demonstrated through the image projection experiments (Figure 7a). Monochromatic or broadband light from the source was passed through a shutter to eliminate unwanted scattering and focus on the selected locations of the fabricated SMLA. The hologram or patterned object was placed before the SMLA. The SMLA was illuminated through a single image/patterned hologram. An array of holographic images were passed through the microscope object lens ( $\times 20$ ,  $\text{NA} = 0.40$ ) and projected over the image screen. Here, honeycomb arrangement of the SMLA was utilized to project holographic images. The bidirectional focusing of the SMLA was valid in image projection experiments. The stepped nanostructure of the

honeycomb arrangement enabled efficient light focusing. This was due to the Bragg effect from the surface relief nano-stepped circular pyramid structures. The light diffracted from the edges of the circles and focused at the center region through constructive interference. For broadband light illumination of an “A” mask, far-field projected images before focusing, at focusing, and after focusing are shown on a screen (Figure 7b–d). For monochromatic light (red, green, and blue), the far-field projected image of “A” was also efficient. However, the light intensity using the blue beam was not clearly captured. Additionally, image projection experiments were also performed through other “insect”, “ball”, and “star” holograms using monochromatic light illumination. The far-field projected hologram images on the screen were uniform in size and shape, which indicated the consistency of the SMLA and high-resolution image focusing.

**Discussion.** We have demonstrated stacked rings having stepped nanostructures that acted as a bidirectional MLA and showed efficient optical focusing. The SMLA fabrication was based on azimuthal multibeam ( $120^\circ$  exposure angles) laser interference holography and roll-to-roll nanoimprinting. The optical properties of the SMLA were characterized through computational modeling followed by experimental analyses. The computed SMLA parameters ( $f$ ,  $f_{\#}$ , and  $\text{NA}$ ) were in agreement with experimental results. Moreover, the performance of the SMLA was comparable with other reported MLAs with lift-off or direct laser writing processes in polymers.<sup>14,50</sup> The light-focusing properties of the SMLA were based on constructive interference from the stepped nanostructures, and its focusing property changed as the step height, width, and number of steps was varied. As the illumination wavelength increased, the fwhm of the focused light increased and linearly shifted to the larger values. Shorter bandwidth and high intensity of the focused light was achieved by decreasing the step height and increasing the number of steps. Moreover, the optical-focusing parameters ( $\text{NA}$ ,  $f$ , and  $f$ -number) were also functions of lens structural parameters.<sup>1</sup> The aspect ratio (height/width) of the fabricated SMLA can be controlled by varying the laser fluence and exposure time. The bidirectional optical-focusing properties of the SMLA were also modeled with FEM analyses and experimentally studied (Supporting Information, Figures S3 and S4).

The optical-focusing properties of the fabricated SMLA were demonstrated with broadband and monochromatic light illumination. Far-field diffraction results were analogous with the reported results.<sup>50</sup> Optical microscope arrangement produced focused diffracted green light upon broadband light normal illumination. The focal distance ( $f = 3.5 \mu\text{m}$ ) of the SMLA was also measured through an optical microscope, which was in agreement with simulated model. The fabricated SMLA also showed maximum  $\text{NA}$  (0.60) as compared to other reported MLAs.<sup>13,14,47</sup> The resolution,  $R$ , is another important optical parameter that determine the image quality and a function of  $\text{NA}$ .<sup>1</sup> Therefore, increases in  $\text{NA}$  values of the SMLA enable higher resolution imaging. Polarization-selective green hotspots were also observed at different points of the hexagonal cells on both sides. Analogous polarization-dependent hotspots were also recently reported.<sup>51</sup> Therefore, the SMLAs also enable the polarization dependent focusing. The optical-focusing properties of the fabricated SMLA were also validated through image projection experiments. However, previously reported MLAs showed focusing property and image/hologram projection experiments only with broadband

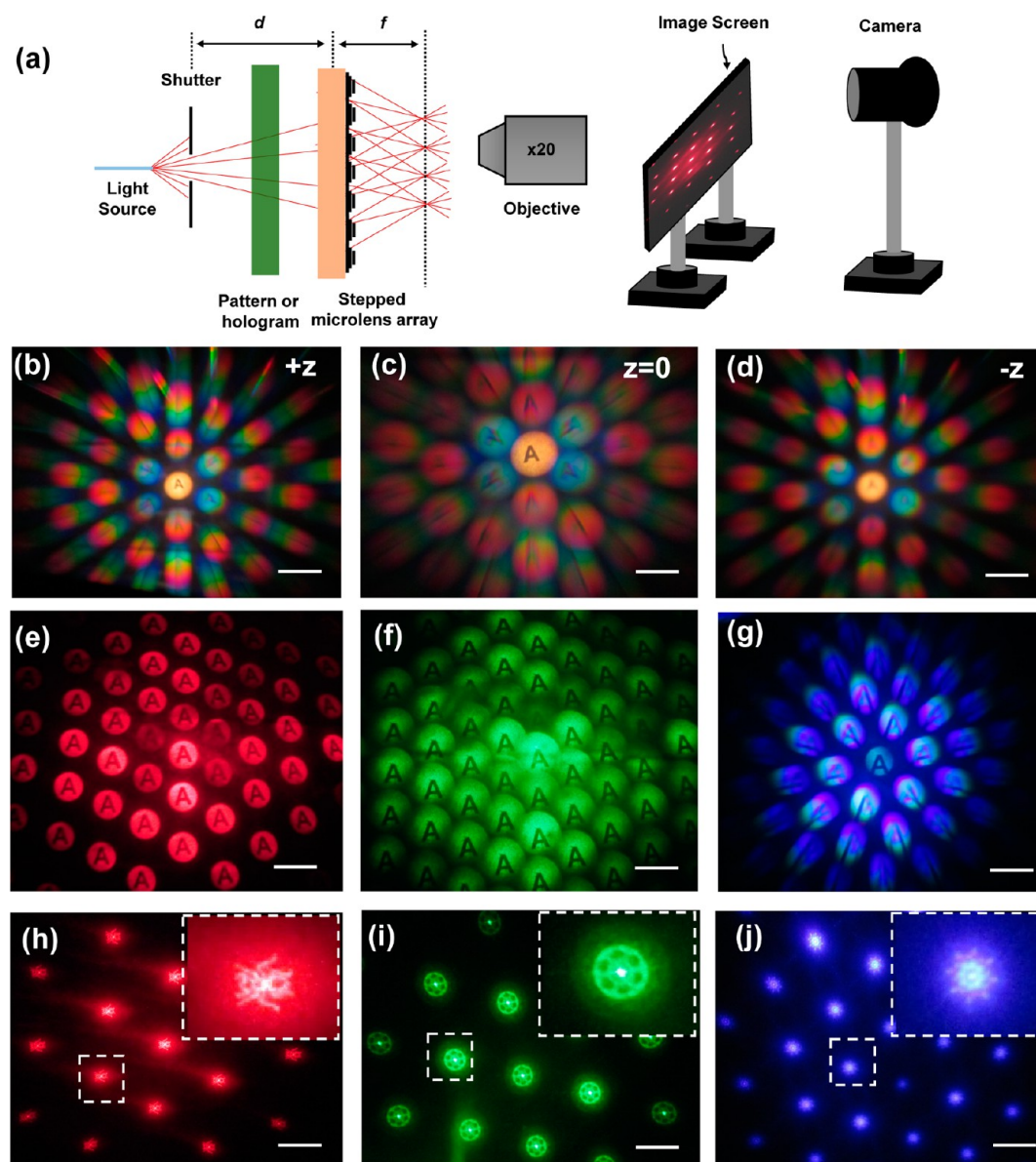


Figure 7. Far-field image/hologram projection experiments. (a) Conceptual block diagram of SMLA for far-field projection experiments. (b–d) For broadband light illumination, distance-dependent far-field projection of text “A” image with focusing ( $z = 0$ ), before ( $-z$ ), and after focusing ( $+z$ ) of SMLA. Scale bars = 2 cm. (e–g) Far-field projection of text “A” image with red, green, and blue light illumination during focused condition of SMLA. Scale bars = 2 cm. (h–j) Far-field projection of holograms: “insect”, “ball”, and “star” images with monochromatic light illumination during focused condition of SMLA. Scale bars = 5 cm.

light and unidirectional focusing.<sup>13,14</sup> The optical-focusing properties were also limited due to low NA values. In the present work, far-field projection experiments were performed with broadband and monochromatic lights, showing bidirectional focusing of the MLA (Supporting Information, Figures S3 and S4). The projection experiments of the SMLA showed multiple copies of text (“A”) and holographic images (“ant”, “ball”, and “star”) from a single copy. Therefore, the capability to copy multiple symbols/information on the SMLA may find applications in data communication and information processing. Each of the SMLA cells focused one image at focal points. The projected images of the SMLA were well-organized and efficient, showing bright focusing that ensured high-resolution imaging capability. The focusing performance of the SMLA was comparable with that of reported devices.<sup>13,14,21</sup> The projection results demonstrated the uniformity and accurate surface

topography of the SMLA (Figure 1b,c). Therefore, the SMLA on flexible AP-PET substrate is suitable for the high-resolution portable imaging applications.

## CONCLUSIONS

In a summary, SMLAs have been fabricated in a close-packed hexagonal configuration on a flexible AP-PET substrate *via* holography and nanoimprinting, and its optical bidirectional focusing properties were demonstrated for broadband and monochromatic light illumination. The performance of the bidirectional SMLA was demonstrated with computational modeling and optical characterization experiments. The optical microscope experiments ensured green light focusing for the broadband light illumination and polarization-dependent green hot spots during unfocused conditions. Far-field projection experiments for the text images or holograms ensured the

SMLA acted as bidirectional lenses. Brightness and uniformity of the far-field projected images indicated highly accurate and well-ordered fabrication the SMLA. It is anticipated the bidirectional SMLAs may find applications in microscale optical devices and miniaturized sensors.

## MATERIALS AND METHODS

**Optical Modeling.** The computational modeling of the SMLAs was performed with COMSOL Multiphysics (v5.2) based on FEM. Light was illuminated on the nanosteped pyramids, and focused light intensity was computed from the other side in a medium defined as air. The pyramid consisted of AP ( $n = 1.49$ ), where height, width, the number of steps were varied, but the thickness of the pyramid was kept constant (30 nm). A hemispherical domain was designed to surround the SMLA. The continuity and scattering boundary conditions were considered for the pyramids and hemispherical surface. The incident light normally illuminated to the SMLA to reduce the angular reflection from the pyramids.

**Stepped Pyramid Fabrication and Nanoimprinting.** The fabrication of the nanosteped pyramid was based on (a) multilayer exposure based on prism coupling, (b) opening exposure, and (c) nanoimprinting from a master hologram. During prism coupling, a multilayer interference pattern was created over the photoresist layer with laser interference (458 nm, maximum exposure angle 50°). Hexagonal stepped circular interference was created during the opening exposure. Three azimuthal beams (458 nm, 100 mW) having 120° exposure angles created an interference pattern in the photoresist to produce stepped circular structures within 1 min. Finally, photographic developer was used to etch the photoresist. To produce multiple copies of the stepped pyramids, a nickel master hologram was used. Multiple copies of the samples were created through a roll-to-roll nanoimprinting process from the nickel master hologram. UV nanolithography was used to print stepped circular pyramids onto AP (2  $\mu\text{m}$ ) over a PET substrate (100  $\mu\text{m}$ ).

**Optical Characterization.** Optical properties of the SMLA were characterized with a spectrophotometer (resolution  $\sim 0.1$ –100 nm fwhm) and a broadband light source (450–1100 nm) purchased from Ocean Optics. Monochromatic red (635 nm, 4.5 mW,  $\varnothing 11$  mm), green (532 nm, 4.5 mW,  $\varnothing 11$  mm), and blue (492 nm, 2.6 mW,  $\varnothing 11$  mm) lasers were purchased from Thorlabs. A computerized stepper motor based 2D X-Y stage (Thorlabs) was used to measure power intensity 180° rotation (step size 1°). Far-field measurements were performed with an image screen (white A4 paper) and a hemispherical surface (semitransparent white,  $\varnothing 30$  cm).

## ASSOCIATED CONTENT

### Supporting Information

The Supporting Information is available free of charge on the ACS Publications website at DOI: 10.1021/acsnano.7b00211.

Laser exposer setup, light focusing property through an optical microscope, bidirectional focusing property, and optical focusing characterization (PDF)

## AUTHOR INFORMATION

### Corresponding Authors

\*E-mail: a.rajib@osamember.org.

\*E-mail: h.butt@bham.ac.uk.

### ORCID

Ali K. Yetisen: 0000-0003-0896-267X

### Author Contributions

R.A. planned for the MLAs project, carried out the experiments and simulations, analyzed results, and wrote the article. A.K.Y. performed SEM and AFM imaging, made intellectual contributions, and edited the article. H.B. supervised the simulations and experiments and led the project.

## Notes

The authors declare no competing financial interest.

## ACKNOWLEDGMENTS

H.B. thanks the Leverhulme Trust for research funding. The authors thank J. Crown and W. Dennis for providing the samples. We also thank Elijah Shirman, Ida Pavlichenko, B. V. Lotsch, and Viola D. for SEM and AFM imaging.

## REFERENCES

- (1) Wu, D.; Wu, S.-Z.; Niu, L.-G.; Chen, Q.-D.; Wang, R.; Song, J.-F.; Fang, H.-H.; Sun, H.-B. High Numerical Aperture Microlens Arrays of Close Packing. *Appl. Phys. Lett.* **2010**, *97*, 031109.
- (2) Yaegashi, M.; Kinoshita, M.; Shishido, A.; Ikeda, T. Direct Fabrication of Microlens Arrays with Polarization Selectivity. *Adv. Mater.* **2007**, *19*, 801–804.
- (3) Hooke, R. *Micrographia: or Some Physiological Descriptions of Minute Bodies Made by Magnifying Glasses, with Observations and Inquiries Thereupon*. Royal Society: London, 1665.
- (4) Gabor, D. Improvements in or Relating to Optical Systems Composed of Lenticules Pat. UK 541,753, 1940
- (5) Daly, D. *Microlens Arrays*; Taylor and Francis: New York, 2000.
- (6) Wu, M. H.; Whitesides, G. M. Fabrication of Diffractive and Micro-optical Elements Using Microlens Projection Lithography. *Adv. Mater.* **2002**, *14*, 1502–1506.
- (7) Kunnavakkam, M. V.; Houlihan, F.; Schlaw, M.; Liddle, J.; Kolodner, P.; Nalamasu, O.; Rogers, J. Low-Cost, Low-Loss Microlens Arrays Fabricated by Soft-Lithography Replication Process. *Appl. Phys. Lett.* **2003**, *82*, 1152–1154.
- (8) Lee, X.-H.; Moreno, I.; Sun, C.-C. High-Performance LED Street Lighting Using Microlens Arrays. *Opt. Express* **2013**, *21*, 10612–10621.
- (9) Abitbol, M.; Eisenberg, N. P. New Process for Manufacturing Arrays of Microlenses on Various Substrates. *Proc. SPIE* **1990**, *1334*, 110–121.
- (10) Wu, M.-H.; Park, C.; Whitesides, G. M. Fabrication of Arrays of Microlenses with Controlled Profiles Using Gray-Scale Microlens Projection Photolithography. *Langmuir* **2002**, *18*, 9312–9318.
- (11) Zhu, Z.; To, S.; Zhang, S. Large-Scale Fabrication of Micro-Lens Array by Novel End-Fly-Cutting-Servo Diamond Machining. *Opt. Express* **2015**, *23*, 20593–20604.
- (12) Hu, W.; Chen, C.; Wu, Y.; Luo, J.; Lei, Y.; Tong, Q.; Zhang, X.; Sang, H.; Xie, C. Graphene-Based Liquid Crystal Microlens Arrays. *Ninth International Symposium on Multispectral Image Processing and Pattern Recognition (MIPPR2015)*; International Society for Optics and Photonics, 2015; 981109–981109-6.
- (13) Lee, K.; Wagermaier, W.; Masic, A.; Kommareddy, K. P.; Bennet, M.; Manjubala, I.; Lee, S.-W.; Park, S. B.; Cölfen, H.; Fratzl, P. Self-Assembly of Amorphous Calcium Carbonate Microlens Arrays. *Nat. Commun.* **2012**, *3*, 725.
- (14) Yong, J.; Chen, F.; Yang, Q.; Du, G.; Bian, H.; Zhang, D.; Si, J.; Yun, F.; Hou, X. Rapid Fabrication of Large-Area Concave Microlens Arrays on PDMS by A Femtosecond Laser. *ACS Appl. Mater. Interfaces* **2013**, *5*, 9382–9385.
- (15) Chan, E. P.; Crosby, A. J. Fabricating Microlens Arrays by Surface Wrinkling. *Adv. Mater.* **2006**, *18*, 3238–3242.
- (16) Kang, D.; Pang, C.; Kim, S. M.; Cho, H. S.; Um, H. S.; Choi, Y. W.; Suh, K. Y. Shape-Controllable Microlens Arrays Via Direct Transfer of Photocurable Polymer Droplets. *Adv. Mater.* **2012**, *24*, 1709–1715.
- (17) Yang, S.; Krupenkin, T. N.; Mach, P.; Chandross, E. A. Tunable and Latchable Liquid Microlenses with Photopolymerizable Composites. *Adv. Mater.* **2003**, *15*, 940–943.
- (18) Im, M.; Kim, D.-H.; Lee, J.-H.; Yoon, J.-B.; Choi, Y.-K. Electrowetting on A Polymer Microlens Array. *Langmuir* **2010**, *26*, 12443–12447.
- (19) Li, X.; Tian, H.; Ding, Y.; Shao, J.; Wei, Y. Electrically Templated Dewetting of A UV-Curable Prepolymer Film for The

Fabrication of A Concave Microlens Array With Well-Defined Curvature. *ACS Appl. Mater. Interfaces* **2013**, *5*, 9975–9982.

(20) Hao, B.; Liu, H.; Chen, F.; Yang, Q.; Qu, P.; Du, G.; Si, J.; Wang, X.; Hou, X. Versatile Route to Gapless Microlens Arrays Using Laser-Tunable Wet-Etched Curved Surfaces. *Opt. Express* **2012**, *20*, 12939–12948.

(21) Chen, F.; Liu, H.; Yang, Q.; Wang, X.; Hou, C.; Bian, H.; Liang, W.; Si, J.; Hou, X. Maskless Fabrication of Concave Microlens Arrays on Silica Glasses by A Femtosecond-Laser-Enhanced Local Wet Etching Method. *Opt. Express* **2010**, *18*, 20334–20343.

(22) Cowan, J. J. Holographic Honeycomb Microlens. *Opt. Eng.* **1985**, *24*, 245796.

(23) Nam, H. J.; Jung, D.-Y.; Yi, G.-R.; Choi, H. Close-Packed Hemispherical Microlens Array from Two-Dimensional Ordered Polymeric Microspheres. *Langmuir* **2006**, *22*, 7358–7363.

(24) Park, E.-H.; Kim, M.-J.; Kwon, Y.-S. Microlens for Efficient Coupling between LED and Optical Fiber. *IEEE Photonics Technol. Lett.* **1999**, *11*, 439–441.

(25) Popovic, Z. D.; Sprague, R. A.; Connell, G. N. Technique for Monolithic Fabrication of Microlens Arrays. *Appl. Opt.* **1988**, *27*, 1281–1284.

(26) Fletcher, D. A.; Crozier, K. B.; Guarini, K. W.; Minne, S. C.; Kino, G. S.; Quate, C. F.; Goodson, K. E. Microfabricated Silicon Solid Immersion Lens. *J. Microelectromech. Syst.* **2001**, *10*, 450–459.

(27) Tien, C.-H.; Hung, C.-H.; Yu, T.-H. Microlens Arrays by Direct-Writing Inkjet Print for LCD Backlighting Applications. *J. Disp. Technol.* **2009**, *5*, 147–151.

(28) Kim, J. Y.; Brauer, N. B.; Fakhouri, V.; Boiko, D. L.; Charbon, E.; Grutzner, G.; Brugger, J. Hybrid Polymer Microlens Arrays with High Numerical Apertures Fabricated Using Simple Ink-Jet Printing Technique. *Opt. Mater. Express* **2011**, *1*, 259–269.

(29) Tripathi, A.; Chronis, N. A Doublet Microlens Array for Imaging Micron-Sized Objects. *J. Micromech. Microeng.* **2011**, *21*, 105024.

(30) Baker, K. M. Highly Corrected Close-Packed Microlens Arrays and Moth-Eye Structuring on Curved Surfaces. *Appl. Opt.* **1999**, *38*, 352–356.

(31) Ahmed, R.; Yetisen, A. K.; El Khoury, A.; Butt, H. Printable Ink Lenses, Diffusers, and 2D Gratings. *Nanoscale* **2017**, *9*, 266–276.

(32) Yetisen, A. K.; Butt, H.; Mikulchik, T.; Ahmed, R.; Montelongo, Y.; Humar, M.; Jiang, N.; Martin, S.; Naydenova, I.; Yun, S. H. Color-Selective 2.5 D Holograms on Large-Area Flexible Substrates for Sensing and Multilevel Security. *Adv. Opt. Mater.* **2016**, *4*, 1589–1600.

(33) Heath, D. J.; Mills, B.; Feinaeugle, M.; Eason, R. W. Rapid Bespoke Laser Ablation of Variable Period Grating Structures Using A Digital Micromirror Device for Multi-Colored Surface Images. *Appl. Opt.* **2015**, *54*, 4984–4988.

(34) Karstens, R.; Gödecke, A.; Prießner, A.; Ihlemann, J. Fabrication of 250-Nm-Hole Arrays In Glass and Fused Silica by UV Laser Ablation. *Opt. Laser Technol.* **2016**, *83*, 16–20.

(35) AlQattan, B.; Butt, H.; Sabouri, A.; Yetisen, A. K.; Ahmed, R.; Mahmoodi, N. Holographic Direct Pulsed Laser Writing of Two-Dimensional Nanostructures. *RSC Adv.* **2016**, *6*, 111269–111275.

(36) Sakellari, I.; Kabouraki, E.; Gray, D.; Purlys, V.; Fotakis, C.; Pikulin, A.; Bityurin, N.; Vamvakaki, M.; Farsari, M. Diffusion-Assisted High-Resolution Direct Femtosecond Laser Writing. *ACS Nano* **2012**, *6*, 2302–2311.

(37) Seo, B. H.; Youn, J.; Shim, M. Direct Laser Writing of Air-Stable p–n Junctions in Graphene. *ACS Nano* **2014**, *8*, 8831–8836.

(38) Chichkov, B. N.; Momma, C.; Nolte, S.; Von Alvensleben, F.; Tünnermann, A. Femtosecond, Picosecond and Nanosecond Laser Ablation of Solids. *Appl. Phys. A: Mater. Sci. Process.* **1996**, *63*, 109–115.

(39) Siddique, R. H.; Hünig, R.; Faisal, A.; Lemmer, U.; Hölscher, H. Fabrication of Hierarchical Photonic Nanostructures Inspired by Morpho Butterflies Utilizing Laser Interference Lithography. *Opt. Mater. Express* **2015**, *5*, 996–1005.

(40) Cowan, J. J. Aztec Surface-Relief Volume Diffractive Structure. *J. Opt. Soc. Am. A* **1990**, *7*, 1529–1544.

(41) Cooper, S.; Tomkins, D.; Petty, M. Surface-Relief Diffraction Gratings Recorded by Multiple-Beam Coherent Phase Exposure. *Opt. Lett.* **1997**, *22*, 357–359.

(42) Rahimi, R.; Ochoa, M.; Ziaie, B. Direct Laser Writing of Porous-Carbon/Silver Nanocomposite for Flexible Electronics. *ACS Appl. Mater. Interfaces* **2016**, *8*, 16907–16913.

(43) Zhou, W.; Bai, S.; Ma, Y.; Ma, D.; Hou, T.; Shi, X.; Hu, A. Laser-Direct Writing of Silver Metal Electrodes On Transparent Flexible Substrates With High-Bonding Strength. *ACS Appl. Mater. Interfaces* **2016**, *8*, 24887–24892.

(44) Kunwar, P.; Hassinen, J.; Bautista, G.; Ras, R. H.; Toivonen, J. Direct Laser Writing of Photostable Fluorescent Silver Nanoclusters in Polymer Films. *ACS Nano* **2014**, *8*, 11165–11171.

(45) Ahmed, R.; Yetisen, A. K.; Yun, S. H.; Butt, H. Color-Selective Holographic Retroreflector Array for Sensing Applications. *Light: Sci. Appl.* **2017**, *6*, e16214.

(46) Cowan, J. J.; Slafer, W. The Recording and Replication of Holographic Micropatterns for the Ordering of Photographic Emulsion Grains in Film Systems. *J. Imaging Sci.* **1987**, *31*, 100–107.

(47) Grunwald, R.; Woggon, S.; Ehlert, R.; Reinecke, W. Thin-Film Microlens Arrays with Non-Spherical Elements. *Pure Appl. Opt.* **1997**, *6* (6), 663.

(48) Ahmed, R.; Rifat, A. A.; Yetisen, A. K.; Dai, Q.; Yun, S. H.; Butt, H. Multiwall Carbon Nanotube Microcavity Arrays. *J. Appl. Phys.* **2016**, *119*, 113105.

(49) Butt, H.; Yetisen, A. K.; Ahmed, R.; Yun, S. H.; Dai, Q. Carbon Nanotube Biconvex Microcavities. *Appl. Phys. Lett.* **2015**, *106*, 121108.

(50) Yabu, H.; Shimomura, M. Simple Fabrication of Micro Lens Arrays. *Langmuir* **2005**, *21*, 1709–1711.

(51) Brooks, L. J.; Mertens, J.; Bowman, R. W.; Chikkaraddy, R.; Sanders, A.; Baumberg, J. J. Polarisation-Selective Hotspots in Metallic Ring Stack Arrays. *Opt. Express* **2016**, *24*, 3663–3671.